



## **Qubit-compatible substrates with superconducting through-silicon vias**

Downloaded from: <https://research.chalmers.se>, 2025-01-15 08:26 UTC

Citation for the original published paper (version of record):

Grigoras, K., Yurttagul, N., Kaikkonen, J. et al (2022). Qubit-compatible substrates with superconducting through-silicon vias. *IEEE Transactions on Quantum Engineering*, 3. <http://dx.doi.org/10.1109/TQE.2022.3209881>








N.B. When citing this work, cite the original published paper.

© 2022 IEEE. Personal use of this material is permitted. Permission from IEEE must be obtained for all other uses, in any current or future media, including reprinting/republishing this material for advertising or promotional purposes, or reuse of any copyrighted component of this work in other works.

Received 5 July 2022; revised 9 September 2022; accepted 17 September 2022; date of publication 26 September 2022; date of current version 17 October 2022.

Digital Object Identifier 10.1109/TQE.2022.3209881

# Qubit-Compatible Substrates With Superconducting Through-Silicon Vias

K. GRIGORAS<sup>1</sup>, N. YURTTAGÜL<sup>1</sup>, J.-P. KAIKKONEN<sup>1</sup>, E. T. MANNILA<sup>1</sup> ,  
P. ESKELINEN<sup>1</sup>, D. P. LOZANO<sup>2</sup> , H.-X. LI<sup>2</sup> , M. ROMMEL<sup>2</sup>,  
D. SHIRI<sup>2</sup> (Member, IEEE), N. TIENCKEN<sup>1</sup> , S. SIMBIEROWICZ<sup>1</sup> ,  
A. RONZANI<sup>1</sup>, J. HÄTINEN<sup>1</sup>, D. DATTA<sup>1</sup>, V. VESTERINEN<sup>1</sup> ,  
L. GRÖNBERG<sup>1</sup> , (Member, IEEE), J. BIZNÁROVÁ<sup>2</sup>,  
A. FADAVI ROUDSARI<sup>2</sup> (Member, IEEE), S. KOSEN<sup>2</sup>, A. OSMAN<sup>2</sup>,  
M. PRUNNILA<sup>1</sup>, J. HASSEL<sup>1</sup>, J. BYLANDER<sup>2</sup>, AND J. GOVENIUS<sup>1</sup>

<sup>1</sup>VTT Technical Research Centre of Finland Ltd., QTF Centre of Excellence, FI-02044 VTT Espoo, Finland

<sup>2</sup>Department of Microtechnology and Nanoscience, Chalmers University of Technology, 412 96 Gothenburg, Sweden

Corresponding author: E. T. Mannila (e-mail: elsa.mannila@vtt.fi).

This work was supported in part by OpenSuperQ, which has received funding from the European Union's Horizon 2020 Research and Innovation Programme under Grant 820363. The work at VTT was supported by the Quantum Computer Codevelopment Project funded by the Finnish government and performed as part of the Academy of Finland Centre of Excellence program under Project 336817, Project 312059, and Project 312294. This work was also supported by the European Commission H2020 project EFINEED under Grant 766853. The Chalmers work was supported in part by the Wallenberg Center for Quantum Technology and performed at Myfab Chalmers. The work of V. Vesterinen was supported by the Academy of Finland under Grant 321700.

**ABSTRACT** We fabricate and characterize superconducting through-silicon vias and electrodes suitable for superconducting quantum processors. We measure internal quality factors of a million for test resonators excited at single-photon levels, on chips with superconducting vias used to stitch ground planes on the front and back sides of the chips. This resonator performance is on par with the state of the art for silicon-based planar solutions, despite the presence of vias. Via stitching of ground planes is an important enabling technology for increasing the physical size of quantum processor chips and is a first step toward more complex quantum devices with 3-D integration.

**INDEX TERMS** High-Q resonator, quantum coherence, superconducting through-silicon via (TSV), tantalum, titanium nitride.

## I. INTRODUCTION

Performance of superconducting qubits has greatly improved since the first demonstrations of quantum coherence, with dephasing time, in particular, increasing four orders of magnitude from 20 ns demonstrated by Chiorescu et al. [1] in 2003 to hundreds of microseconds measured recently [2], [3], [4], [5]. To an extent, this astonishing progress in coherence time has been achieved by avoiding complexity in fabrication. State-of-the-art superconducting qubits are typically fabricated using an extremely restricted set of materials, a low thermal budget, and a minimal number of depositions and lithographic steps.

Besides long coherence times required to achieve high-fidelity single- and two-qubit gates, quantum computers also need to become sufficiently large to solve useful computing tasks. For example, tens or hundreds of millions of physical qubits are likely required for factoring thousand-bit numbers using Shor's algorithm [6] and similar estimates have been

given for quantum chemistry applications [7]. These estimates assume error correction based on the surface code [8], which is currently the most promising approach to quantum error correction. One attractive feature of the surface code is that it requires only 2-D nearest-neighbor coupling between qubits, which makes a physical implementation of a large quantum computer more feasible. Nevertheless, separate control and readout lines still need to address essentially all of the qubits. Routing the control and readout lines around coherent qubit couplers necessitates the use of more than a single electrode layer in larger quantum processors. Consequently, moving to more complex fabrication seems unavoidable, either monolithically or by using multi-chip modules. Flip-chip bonded modules of two chips connected by superconducting bumps increase the layer count to two and air bridges further alleviate routing challenges. These have indeed been used successfully to construct processors of several dozen qubits [9], [10], [11], although with

coherence times and gate fidelities significantly lower than in planar [12], [13], [14], [15], [16] or flip-chip bonded [17] single- or few-qubit devices.

Superconducting vias compatible with high-coherence qubits are an important next step toward larger processors. In addition to routing purposes, so-called via stitching is likely needed to shunt nominally grounded planes in different layers to control and push up the frequencies of harmful parasitic microwave modes that become problematic in physically large chips [18]. Traditional integrated circuit vias are, however, optimized for different goals, such as high normal-state conductivity and reduction of parasitic capacitance, instead of superconductivity and extremely low microwave loss required for qubit compatibility. Integrating their fabrication with qubits also poses challenges related to material compatibilities and the low thermal budget of aluminum-based qubits. Superconducting vias have long been used for multilayer wiring in superconducting quantum interference and single-flux quantum devices [19], [20], but the vias are shallow and pass through amorphous dielectric layers with poor microwave performance.

Yost et al. [21], [22] have, on the other hand, demonstrated through-silicon vias (TSVs) that have a relatively high aspect ratio and high critical currents and show promise in terms of not destroying qubit coherence, as the demonstrated qubit relaxation time of  $12.5 \mu\text{s}$  [21] and resonator internal quality factors of  $10^5$  to  $2 \times 10^5$  [22] were identified to be limited by factors unrelated to TSVs. For comparison, widely reproduced relaxation times for transmon qubits on silicon substrates are near  $50 \mu\text{s}$  [12], [13], [14], [15], [16], [17]. In addition, Gordon et al. [4] have reported relaxation times of hundreds of  $\mu\text{s}$ . Corresponding widely reproduced resonator quality factors are roughly one million for typical coplanar waveguide (CPW) test resonator geometries [13], [14], [23], [24], [25], although this can be exceeded with deep trenching or short-lived oxide removal treatments [26], [27], [28]. Resonator quality factor is often used as a diagnostic predictor of qubit relaxation time for a qubit with electrodes fabricated using the same flow as the resonators. Others have also fabricated superconducting TSVs, but the microwave performance of those approaches remains to be measured [29], [30], [31]. Furthermore, coherence times exceeding  $300 \mu\text{s}$  have recently been demonstrated for transmon qubits on planar sapphire substrates [2], [3]. However, typical methods of etching high aspect ratio TSVs, like the Bosch process [32], [33], are not available for sapphire substrates.

In this article, we report on resonator internal quality factors of roughly a million measured on chips with TSVs stitching the ground planes on the front and back. The TSVs and resonators are fabricated on full 150-mm wafers, with a via-last approach where the first electrode layer is deposited and patterned before via formation. The via-last approach helps create a high-quality interface between the substrate and the critical electrode layer used for the resonators since the electrode layer is deposited on virgin wafers before other potentially harmful processing steps. Furthermore, the

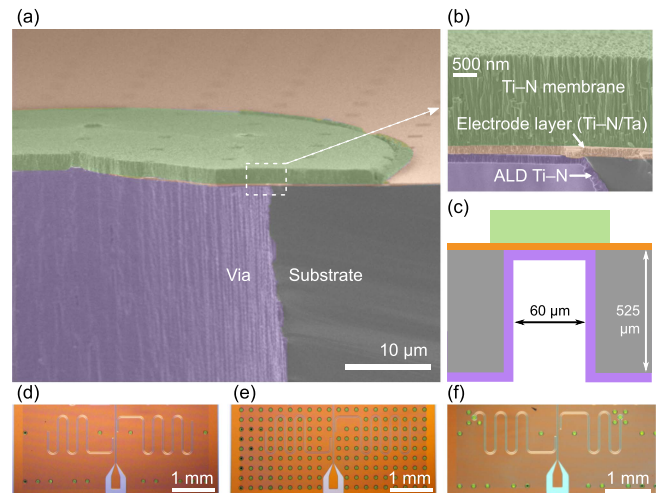


**FIGURE 1.** (a) and (b) False-color scanning electron microscope images of a TSV. (c) Schematic cross section of TSV structure (not to scale), with color-coding as in (a) and (b). (d)–(f) Optical micrographs showing layouts of CPW test resonators with different densities and roles of TSVs (green circles). (d) Sparse via stitching. (e) Dense via stitching. (f) TSV-terminated resonators.

tantalum-based electrode layer used here has relatively low kinetic inductance, similar to commonly used niobium films. While high kinetic inductance is useful in superinductors, for example, in the fluxonium shunt inductor [34], kinetic inductance in electrodes of transmon qubits is not typically desirable. Low kinetic inductance tends to also yield better parameter control since geometric inductance is often more accurately reproducible than kinetic inductance, which tends to be very sensitive to variations in chemical composition and crystal structure.

## II. DEVICE STRUCTURE

Fig. 1 presents our TSV structure consisting of the main electrode layer on the front side of the wafer, a hollow via with metallized walls, a metal membrane covering the via on the front side of the wafer, and a metallized back side (not visible). The fabrication process begins with sputtering the main electrode layer, i.e., a bilayer of 15 nm of titanium nitride and 200 nm of tantalum (orange in Fig. 1), on high-resistivity silicon. For brevity, we refer to this as the Ta-based electrode layer. We then pattern the electrode layer using photolithography and plasma etching. Next we deposit a sacrificial silicon dioxide layer using plasma-enhanced chemical vapor deposition and pattern holes in it for the membranes, using photolithography and plasma etching. We then sputter a  $2\text{-}\mu\text{m}$ -thick titanium nitride layer and pattern it into circular membranes using photolithography and plasma etching (green in Fig. 1). We choose membrane sputtering parameters that yield relatively low compressive stress of approximately 190 MPa, as measured on 250-nm-thick reference films. Next we define the via holes on the back side of the wafer using photolithography and etch them using the Bosch process. Finally, we coat the inner walls of the vias and the

back side of the wafer with Ti–N by using plasma-enhanced atomic layer deposition (ALD, purple in Fig. 1), and remove the sacrificial silicon oxide layer from the front side. The ALD film thickness is 260 nm, as measured on the back side of the wafer. As seen in Fig. 1(b), the film is noticeably thinner at the other end of the via (ca. 200 nm), as is typical for plasma-enhanced ALD processes.

The aspect ratio of our TSVs is approximately eight, with a nominal TSV diameter of 60  $\mu\text{m}$  and substrate thickness of 525  $\mu\text{m}$ . The aspect ratio is similar to that of [21] and [22]. It should be possible to increase the aspect ratio in the future since the only coating needed inside the vias is produced by ALD, which is highly conformal compared to most deposition methods. Furthermore, a smaller via diameter is likely achievable with thinner wafers, even without increasing aspect ratio. Smaller-diameter vias enable increased via density and are likely to lead to increased mechanical robustness of the metal membranes covering the vias. Increased via density is likely to be beneficial in the future, when footprint per qubit decreases below current typical values of roughly 0.5  $\text{mm}^2$ . Increased mechanical robustness on the other hand improves postprocessability. Currently, the membranes survive typical wafer-level handling and processing, but the suspended parts of the membranes are susceptible to being cleaved off when the wafers are diced into chips. The suspended part of the membrane is inconsequential from the point of view of electrical connectivity; so this is not a significant issue for the resonator samples characterized here, but the fragility of the membranes may be an inconvenience in some applications requiring postprocessing on diced chips. Optimizing the stress of the membrane layer to optimally pretension the membrane could be another future path toward improving mechanical robustness.

Our measurements and results focus on CPW resonators patterned on chips with TSVs, to demonstrate long relaxation time in the presence of TSVs. We compare these to planar reference chips with resonators patterned on Nb, or on the same Ta-based electrode layer as on the TSV chips. The TSV chips have two to eight CPW resonators coupled to a common feedline through which transmission is measured (see Fig. 1). Each resonator acts as a bandstop filter at each of its resonance frequencies and thus provides a sensitive probe of microwave loss at those frequencies, assuming the internal quality factor  $Q_i$  and coupling quality factor  $Q_c$  are of similar order of magnitude. Here, the resonators are open near the feedline and shorted at the opposite end, with geometry chosen such that the fundamental  $\lambda/4$  resonance frequency varies between 4 and 8 GHz and the coupling quality factor between  $2 \times 10^4$  and  $7 \times 10^6$ . The width of the CPW center trace is 20  $\mu\text{m}$  and the gap between the center and ground is 10  $\mu\text{m}$ , as in [25]. Overetching past the metal layer is small, less than roughly 50 nm, and no additional trenching is applied. The exact dimensions of the CPW cross section play a significant role when making direct quantitative comparisons since, in extremely low-loss resonators, losses are generally dominated by material imperfections in thin interface layers

between different materials, and the participation factors of different interfaces are somewhat geometry dependent [23], [35], [36], [37].

In terms of density and role of TSVs, we use the following four types of layouts:

- 1) no TSVs and no ground plane on the back, used as reference;
- 2) sparse TSVs stitching the ground planes on the front and back;
- 3) dense TSVs stitching the ground planes;
- 4) sparse TSVs stitching the grounds and TSVs terminating the resonators to the ground plane on the back.

As shown in Fig. 1(d), the sparse TSV design (2) has a spacing of 0.5–2 mm between the TSVs in areas near the resonators, with each resonator having 1–3 stitch vias at a distance of 150–300  $\mu\text{m}$  from the center trace. This design aims to minimize the currents and electric fields induced in the vias when the resonators are excited, while still providing sufficiently dense via stitching for the ground planes to increase the frequency of the parasitic chip modes above the measurement band. The dense TSV design (3), with a TSV spacing of only 0.23 mm [Fig. 1(e)], greatly increases the participation of the stitch vias in the resonant modes by increasing their number and proximity to the center trace. The TSV-terminated design (4) [Fig. 1(f)] makes TSVs an integral part of the resonator, with the termination consisting of one TSV for the center conductor and three or four TSVs for the ground. On the back side of the chip, the ends of the terminating TSVs are approximately at a voltage node of the resonator, but the nonnegligible physical and electrical length of the vias implies that the ends of the vias on the front side are roughly  $0.02\lambda$  away from the voltage node.

### III. QUALITY FACTOR MEASUREMENTS

Fig. 2(a) shows that the best resonator chips with sparse TSVs stitching the front and back ground planes reach internal quality factors exceeding  $10^6$  at single-photon powers circulating in the resonator. The mean photon number in the resonator is nearly linearly proportional to the input probe power. In panel (a), we show the power dependence for a few exemplary resonators, and panels (b) and (c) show the low-power  $Q_i$  for all resonators on the measured chips. Details of the measurement setup, samples, and data analysis are given in Appendices A and B. The resonators with sparse stitch vias perform approximately identically to planar reference resonators fabricated on either the same tantalum-based electrode layer [Fig. 2(d)] or niobium [Fig. 2(e)]. Furthermore, the resonator performance is similar to other reported results for silicon substrates [13], [14], [23], [24], [25] and suggests that transmon-type qubits patterned on the same electrode layer can achieve state-of-the-art coherence. This is the main result reported in this article as it demonstrates that none of the processing steps required to form the TSVs is fundamentally detrimental to the coherence. Even though the TSVs are not strongly coupled to the most sensitive long-coherence elements on the chip, the fact that via stitching of the ground



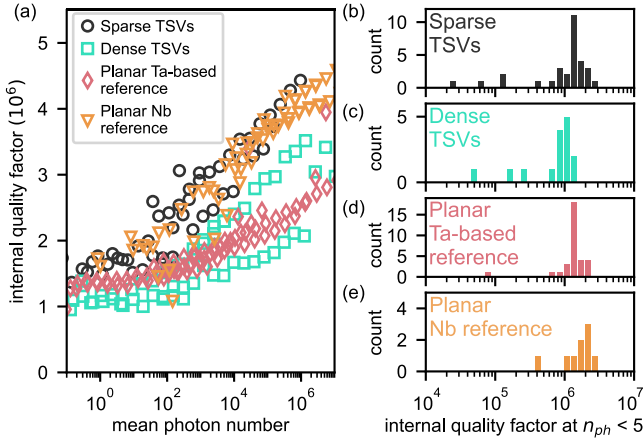


**FIGURE 2.** Quality factor measurements for via-stitched TSV chips. (a) Measured internal quality factors  $Q_i$  at 10 mK as a function of photon number  $n_{ph}$  circulating in the resonator for resonators with sparse stitch TSVs (black circles), dense stitch TSVs (green squares), planar reference resonators with the same Ta-based electrode layer (diamonds), and planar reference resonators with an Nb electrode layer (triangles). For clarity, data are shown for only two resonators with frequency between 4 and 5.5 GHz for each device type. (b)–(e) Histogram of measured internal quality factors at low photon numbers for all measured resonators of the types shown in panel (a).

planes can be compatible with high-coherence qubits is an important advancement in itself, as it allows physically larger quantum processor chips.

We draw this conclusion by comparing the best TSV chips to the best reference chips, which are on par. However, certain uniformity and yield issues remain to be solved. This can be seen in the histogram in Fig. 2(b) showing a small fraction of outlier resonators with anomalously low quality factors, which are relatively power independent. We occasionally find such outliers also in both Ta- and Nb-based planar reference devices. Furthermore, resonators near the edges of the 150-mm wafers show  $Q_i$  below  $10^5$ , even for the sparse TSV test design. In this article, we exclude the edge chips, as wafer-level uniformity of the process has not yet been a development priority and we assume that it can be improved in the future.

We observe somewhat decreased  $Q_i$  in chips with dense stitch vias [Fig. 2(a)]. Furthermore, in resonators terminated with TSVs, the internal quality factors are drastically lower, ranging from  $Q_i$  less than  $10^4$  to  $2 \times 10^5$ , as shown in Fig. 3. The line shapes of TSV-terminated resonators also generally become asymmetric at just  $10^3$ – $10^5$  photons, after which the model used to extract  $Q_i$  from the response [38] no longer fits well. In resonators without TSV terminations, we observe such a threshold only above powers corresponding to over  $10^7$  photons. Furthermore, TSV-terminated resonators show essentially no power dependence of  $Q_i$ , until the nonlinearity leading to asymmetric response becomes significant.

These observations suggest that, unlike in the resonators with  $Q_i$  in the range of a million, two-level systems (TLSs) in thin dielectric interface layers are not a significant loss mechanism for the TSV-terminated resonators, as they would

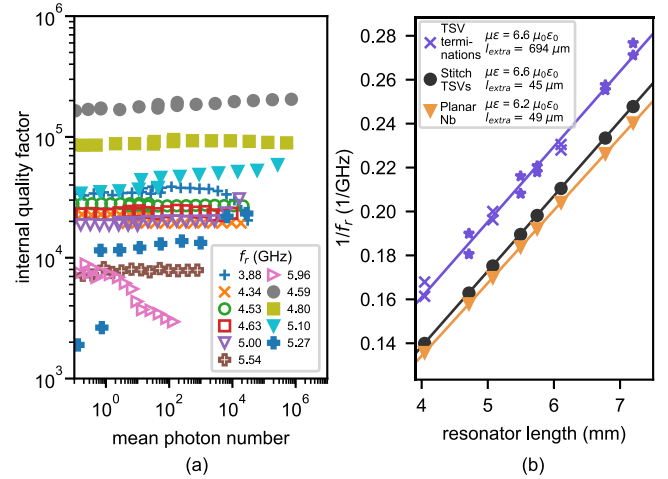


**FIGURE 3.** (a) Internal quality factor versus photon number for TSV-terminated resonators. Data points at high powers are not shown due to poor fit of the model to asymmetric line shapes at high powers, and data is not shown for those resonances where  $Q_i \ll Q_c$  leading to large uncertainty in fitting. (b) Inverse resonance frequencies of several chips with TSV-terminated resonators (crosses and stars), resonator with sparse via stitching (circles), and reference Nb resonators (triangles) versus length of the coplanar part. Crosses (stars) indicate a TSV termination with three (four) ground vias around the terminating TSV. Solid lines indicate fits to (1) with parameters given in the legend.

be expected to lead to quality factors increasing with photon number. It is instead possible that the ALD titanium nitride film on the inner walls of the hollow TSVs contains weak spots with suppressed superconductivity. This should lead to rapid decrease of quality factor at powers where the current through the termination becomes comparable to the critical current of the weak spot. We estimate that, at the threshold power for asymmetric response, the current through the TSV terminations is on the order of  $10 \mu\text{A}$  (see Appendix B). Such stochastically occurring weak spots could explain the large variation in  $Q_i$ , as well. It is also possible that resistive losses occur at the interface between the ALD titanium nitride and the sputtered electrode layer. Nevertheless, the best TSV-terminated resonators perform as well as the TSV-interrupted resonators in [22].

The resonance frequencies  $f_r$  of the TSV-terminated resonators are consistent with those of other resonators, after accounting for approximately  $650 \mu\text{m}$  of CPW-equivalent length added by the TSV terminations. The added length is qualitatively consistent with a wafer thickness of  $525 \pm 25 \mu\text{m}$  and a higher effective dielectric constant within the TSV termination, as compared to the CPW part. To demonstrate this, Fig. 3(b) shows inverse resonance frequency versus resonator length  $l_{\text{design}}$  for different resonator types, as well as fits to

$$1/f_r = 4\sqrt{\mu\epsilon}(l_{\text{design}} + l_{\text{extra}}) \quad (1)$$

where the speed of light in the CPW  $1/\sqrt{\mu\epsilon}$  and extra CPW-equivalent length  $l_{\text{extra}}$  are fit parameters. Neglecting kinetic inductance and film thickness [39], we expect  $\mu\epsilon =$

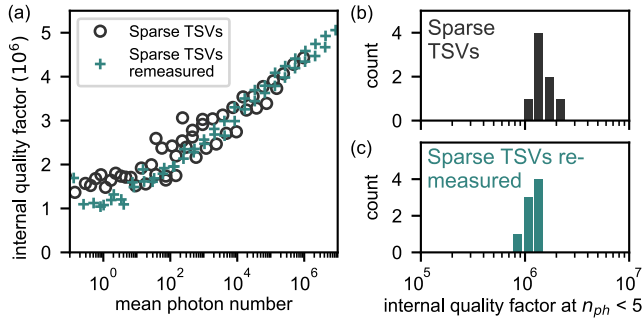


**FIGURE 4.** (a) Internal quality factor versus photon number for sparse TSV resonators (black circles) compared to the same device measured two weeks later (stars). For clarity, only two resonance frequencies are shown per device. (b) and (c) Histograms of low-power  $Q_i$  for the chips shown in panel (a).

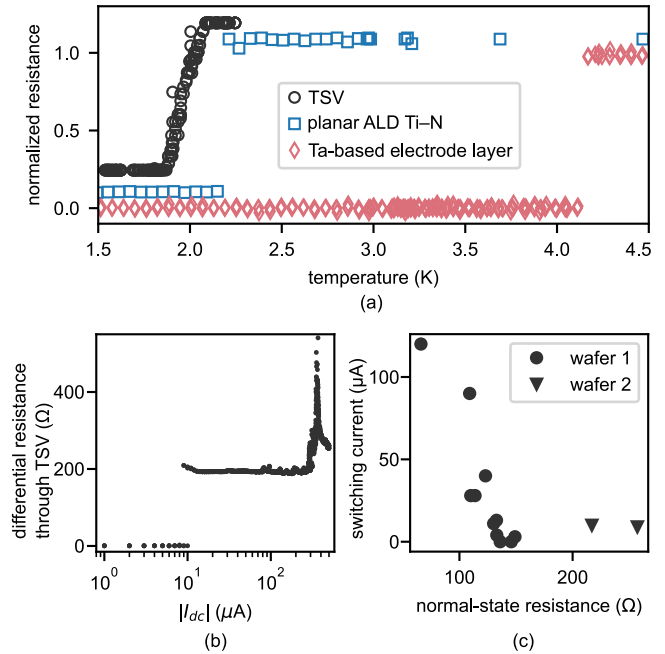
$6.23\mu_0\epsilon_0$  for our CPWs, assuming  $\epsilon_r = 11.45$  for the permittivity of silicon [40]. For chips with stitch vias only, as well as for planar reference chips, the measured frequencies of individual resonators deviate from the linear fit by less than 0.05%. For TSV-terminated resonators, however, the scatter is relatively large, showing an average deviation of 2% even within a single chip. The variation in the resonance frequencies from the prediction of the linear fit is not explained by variation in the termination design [three vs. four grounding TSVs surrounding the via terminating the center conductor; see Fig. 1(f)]. Fig. 3(b) also shows that the resonance frequencies of resonators with stitch vias only are similar to those of planar resonators patterned on a reference Nb film. This demonstrates the low kinetic inductance of the tantalum-based electrode layer and therefore high compatibility with typical Nb-based designs for superconducting qubits.

Fig. 4 shows that a chip with sparse TSV stitching continues to show internal quality factors of  $10^6$  even after the chip is left at room temperature and atmospheric pressure for two weeks after the initial measurements. This is consistent with our observation (not shown) that planar reference samples with the same tantalum-based electrode layer are also stable in time.

Power dependence of  $Q_i$  is commonly used to estimate the contribution of TLS losses, as most other loss mechanisms are expected to be independent of power at these powers. All of the resonator types in Fig. 2(a) show relatively weak power dependence and lack clear saturation of  $Q_i$  at high powers, making accurate estimation a challenge. Here, we use the common simplistic approach of defining the total TLS loss  $F\delta_{\text{TLS}}^0$  as  $\delta_{\text{LP}} - \delta_{\text{HP}}$ , where  $\delta_{\text{HP}}$  ( $\delta_{\text{LP}}$ ) is defined as  $1/Q_i$  at the highest (lowest) measured power. The obtained value  $F\delta_{\text{TLS}}^0 \simeq 5 \times 10^{-7}$  is of the same order of magnitude as best reported results for planar devices [23].

#### IV. DC CHARACTERIZATION

The superconducting transition temperature of the tantalum-based electrode layer is slightly above 4 K [Fig. 5(a)], in



**FIGURE 5.** (a) Temperature dependence of normalized resistance for ALD titanium nitride inside a single via (circles), planar ALD titanium nitride (squares), and the planar tantalum-based electrode layer (diamonds). For clarity, the traces are offset vertically in steps of 0.1. (b) Differential resistance versus the absolute value of bias current  $I_{\text{dc}}$  through a single TSV at 100 mK, showing several switching currents. The response is symmetric around  $I_{\text{bias}} = 0$ . (c) Smallest switching current versus normal-state resistance for several different TSVs on two wafers.

line with a literature value of 4.46 K for high-purity bulk tantalum [41]. On the planar back side of the wafer, the ALD titanium nitride coating has a transition temperature in excess of approximately 2 K, which is typical for highly disordered titanium nitride deposited by ALD. The critical temperature is significantly below highest values achieved with ALD or other methods (4.5–5.4 K) [42] but easily satisfies the basic requirement of effectively suppressing thermal quasiparticles in superconducting qubit applications, which operate around 10–30 mK. The critical temperatures and currents were measured with standard lock-in techniques in a four-probe configuration (see Appendix B for details).

The transition of titanium nitride to the superconducting state is significantly broadened toward lower temperatures when measured through a TSV, as shown in Fig. 5(a). This is qualitatively similar to the broad transition measured through TSVs lined with titanium nitride by Mallek et al. [22]. Furthermore, Fig. 5(b) shows that the via switches from the superconducting state to the normal state gradually, in multiple steps from tens to hundreds of  $\mu\text{A}$ , and the lowest switching current varies from a few microamperes to over 100  $\mu\text{A}$  [Fig. 5(c)]. Both the broad superconducting transition over temperature and observation of multiple critical currents are consistent with the existence of weak spots in the titanium nitride lining inside the via. The weakest spot determines the lowest switching current and, due to Joule heating, also likely limits the highest observed switching currents to only

hundreds of  $\mu\text{A}$ , which correspond to only a few  $\text{kA}/\text{cm}^2$  of nominal current density. The measured critical currents are also of similar magnitude as the current through the TSVs at the threshold power where the lineshapes of TSV-terminated resonators become asymmetric (Fig. 3).

## V. CONCLUSION

In conclusion, we successfully fabricated and characterized qubit-compatible microwave resonators on silicon wafers with TSVs stitching the front and back ground planes. The measured resonator internal quality factors improve over previous results [22] by nearly an order of magnitude and are on par with fully planar resonator results, despite the added complexity of fabrication. The resonator performance provides strong evidence that state-of-the-art qubit coherence times would likely be reached if the same process were used for transmon-type qubits, with Josephson junctions postprocessed on the samples using established evaporation-based methods. Stitching the ground planes with TSVs is an important technique for controlling parasitic microwave modes within the silicon chip. Without TSVs or other methods for controlling them, the parasitic modes limit the physical size of transmon-based quantum processor chips to the range of two centimeters. Qubits fabricated on sapphire substrates have shown even better performance, but there is no clear path to fabricating qubit-compatible high-aspect-ratio vias on sapphire substrates.

Critical currents of the TSVs demonstrated here leave room for future improvement. The low switching currents in dc measurements, the existence of outliers in the microwave measurements, and the dramatically lower performance of TSV-terminated resonators all hint in the direction of weak spots in the titanium nitride film inside the vias. This may be due to roughness of the via walls or due to imperfect conformality of the plasma-enhanced ALD process, which could lead to variation in film quality and weaker superconductivity at the far end of the via. Alternatively, the losses may be due to poor contact between the ALD titanium nitride and the sputtered titanium nitride in the electrode layer. These potential issues can be improved without drastic changes to the TSV structure. Together with additional patterning of the back side metallization, improving critical currents to the mA range would make the TSVs applicable to flux line routing. The low critical currents observed here limit the applications to grounding, charge excitation lines, and readout lines. Other possible future improvements include increasing the aspect ratio of the vias or reducing the thickness of the wafers, which would both lead to smaller diameter vias. Smaller diameter vias increase integration density and would improve the mechanical stability of the membranes covering the TSVs.

## APPENDIX A RESONATOR DESIGNS AND SAMPLES

The results presented in this manuscript are obtained from measurements of over 100 resonators on 15 chips in

several cooldowns. The measured resonators are  $\lambda/4$  CPW resonators in a hanger-type configuration [43]. Transmission measurements in this configuration lead to a Lorentzian dip in the response and allow taking cable losses and impedance mismatch into account by normalizations of the measurement data with well-established models [23], [38], [44].

Each chip hosts up to ten resonators with differing lengths. The resonators are either capacitively coupled to a common microwave feedline on one end and shorted to ground at the opposite one, or inductively coupled to the feedline with the opposite end left open. All designs have a  $20\text{-}\mu\text{m}$  wide CPW center trace and  $10\text{-}\mu\text{m}$  gap between the center pin and ground electrodes and incorporate a square grid of flux trapping holes in the ground planes. The measured designs differ in the presence and role of TSVs and backside metallization, as well as the precise lengths of the resonators and couplings to the feedline. The design parameters along with the coupling quality factors  $Q_c$  obtained from fitting the data are summarized in Table 1. The resonator lengths range between 4 and 7 mm for all designs.

In Table 2, we list the resonator chips and their measurement configurations. All resonances on all the listed chips are included in the  $Q_i$  histograms shown in Fig. 2 of the main text. Fig. 4 shows measurements of chip S2 in two cooldowns. We have excluded measurements performed without magnetic shielding as well as chips from the edges of the wafers from the manuscript. In Fig. 3, we include only those resonances where the resonator fitting (described below) produced a reliable result.

## APPENDIX B MEASUREMENTS AND DATA ANALYSIS

### A. DC MEASUREMENTS

For the dc characterization results shown in Fig. 5, test chips were glued to an insulating sapphire chip which was, in turn, mounted with vacuum grease to a copper sample holder thermally anchored to the mixing chamber stage of a dilution refrigerator. The critical temperatures of the tantalum-based electrode layer and ALD titanium nitride were measured in standard four-probe configurations with a lock-in amplifier. The measurement configuration used in the measurements of individual TSVs is schematically shown in Fig. 6. For the critical current measurements shown in Fig. 5(c), the refrigerator temperature was stabilized to approximately 100 mK with a PID controller, as the dissipation from the TSVs in the normal state is significant compared to the cooling power of the refrigerator.

### B. RESONATOR MEASUREMENTS

For the resonator measurements, we wire bond chips to sample holders machined from copper or gold-plated copper thermally anchored to the mixing chamber plate of a dilution refrigerator. The sample holders are mounted inside magnetic shields consisting of a mu-metal shield and a superconducting aluminum tube. In most of the measurements,

**TABLE 1 Resonator Designs Used in the Article**

Design	Role of TSVs	Backside metallization	Number of resonators on chip	$Q_c$	Chip size (mm × mm)	Flux trapping hole diameter (μm)	Flux trapping hole spacing (μm)	Coupling to feedline	Note
Sparse TSVs 1	Stitch vias 150 to 300 μm from resonators	yes	8	$2 \times 10^4$ to $2 \times 10^5$	$5 \times 7$	2	10	capacitive	Resonator lengths and couplings identical to sparse TSVs 1
Sparse TSVs 2	Stitch vias 150 to 500 μm from resonators	yes	2	$2 \times 10^6$ to $8 \times 10^6$	$14.3 \times 14.3$	2.5	8	inductive	
Dense TSVs	Stitch vias 100 μm from resonators	yes	8	$2 \times 10^4$ to $2 \times 10^5$	$5 \times 7$	2	10	capacitive	
TSV-terminated resonators	Stitch vias 150 to 300 μm from resonators, resonators terminate in TSVs	yes	8	$2 \times 10^4$ to $2 \times 10^5$	$5 \times 7$	2	10	capacitive	
Reference A	None	no	8	$2 \times 10^4$ to $2 \times 10^5$	$5 \times 7$	2	10	capacitive	
Reference B	None	no	8	$1 \times 10^4$ to $2.5 \times 10^6$	$5 \times 5$	2.5	8	inductive	Resonator lengths and couplings identical to sparse TSVs 1
Reference C	None	no	10	$2 \times 10^5$ to $5 \times 10^6$	$5 \times 7$	2.5	8	inductive	

All resonators have a 20-μm wide CPW center trace and 10-μm gap between the center pin and ground electrodes. All designs incorporate a square grid of flux trapping holes. The design Reference A was only used to obtain the reference data for resonance frequencies in Nb resonators shown in Fig. 3 of the main text.

**TABLE 2 Samples for Which Data is Presented in the Article**

Sample	Wafer	Design	Sample holder	Notes
S1	TSV1	Sparse TSVs 1	Cu	
S2	TSV1	Sparse TSVs 1	Cu	
S3	TSV1	Sparse TSVs 1	Cu	
S4	TSV2	Sparse TSVs 2	Cu	Base temperature 30 mK
S5	TSV2	Sparse TSVs 2	Cu	Base temperature 30 mK
S6	TSV2	Sparse TSVs 2	Cu	Base temperature 30 mK
D1	TSV1	Dense TSVs	Cu	
D2	TSV1	Dense TSVs	Au/Cu	Only 10 dB attenuation at mixing chamber
T1	TSV1	TSV-terminated resonators	Cu	
T2	TSV1	TSV-terminated resonators	Au/Cu	Only 10 dB attenuation at mixing chamber
R1	Ta	Reference B	Au/Cu	
R2	Ta	Reference B	Au/Cu	
R3	Ta	Reference B	Au/Cu	Base temperature 40 mK
R4	Ta	Reference B	Au/Cu	Base temperature 40 mK
R5	Nb	Reference C	Cu	

Wiring is only specified if it differs from the setup shown in Fig. 7. Base temperature is only specified if it exceeded 15 mK.

the magnetic shields are mounted inside a radiation shield thermalized to the mixing chamber flange, but we have not observed significant differences between samples measured inside or outside the mixing chamber shield. For most of the measurements, the base temperature of the refrigerator was below 15 mK, with exceptions indicated in Table 2.

The measurement setup used is schematically depicted in Fig. 7. The probe signal is generated by a vector network analyser (VNA) at room temperature. The VNA output is

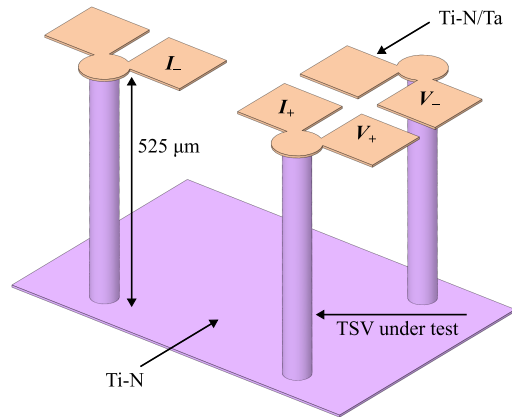


**FIGURE 6. Schematic of the four-probe arrangement for measuring critical currents and temperatures through individual TSVs. Each via is connected to individual bond pads on the front side of the wafer, and the same unpatterned metallization on the back side.**

connected to one of two attenuated and filtered coaxial lines used for either transmission or reflection measurements. In the transmission configuration, the attenuated signal is connected to the input port of the device under test (DUT), while the reflection measurement line is connected to the other port of the DUT with a circulator. However, in this work, we only present transmission measurements. To estimate the power reaching the DUT, we have measured the transmission through two identically attenuated coaxial lines connected in series at the base temperature of the refrigerator. We use this reference data as well as datasheet values for the frequency-dependent attenuation of room temperature cables



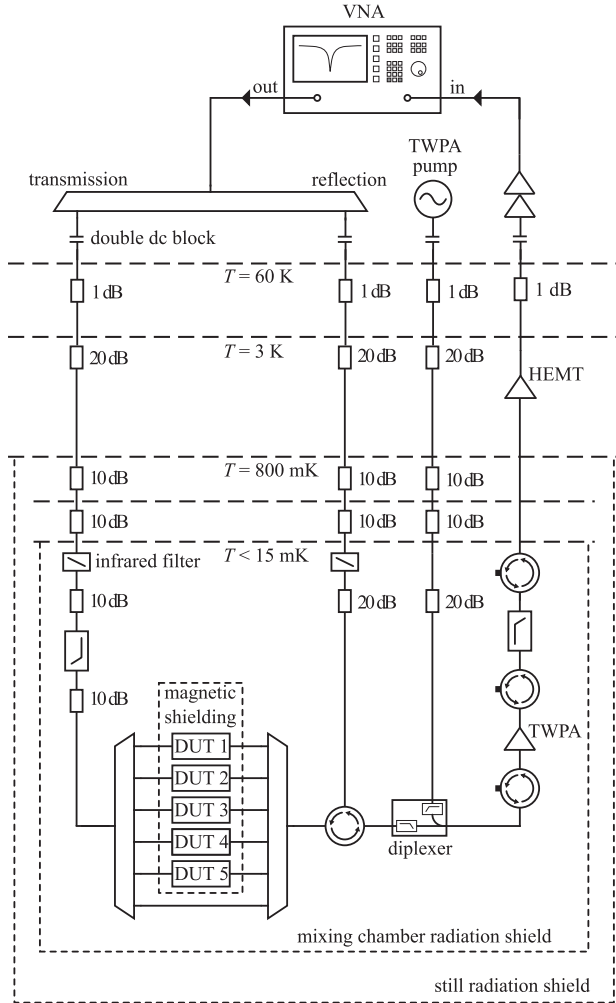


**FIGURE 7.** Measurement setup used for microwave measurements. The low-pass filters in the transmission and output lines have a cutoff frequency of 12.5 GHz. The infrared filters in the transmission and return loss lines are Eccosorb filters with a low insertion loss in the 4–8 GHz band. The passband of the circulators and isolators is 4–12 GHz. The control lines of the microwave switch at the mixing chamber or flux bias connections to the traveling wave parametric amplifier are not shown.

and components to calculate the power reaching the DUT. Slight differences in the attenuation or filtering between cooldowns are indicated in Table 2.

We use a pair of microwave switches at the mixing chamber to allow characterizing up to five DUTs in a single cooldown, as well as a coaxial cable that can be used as a transmission reference. The transmitted signal is amplified with a near quantum limited three-wave mixing traveling wave parametric amplifier (TWPA) at the mixing chamber stage and high-electron-mobility transistor (HEMT) amplifiers at 4 K and at room temperature. The pump tone for the TWPA with frequency typically close to 14 GHz is combined with the signal from the DUT with a diplexer and filtered again from the signal after the TWPA stage to avoid saturation of the following amplifiers, while several isolators provide isolation between the DUT and the TWPA and

TWPA and HEMT amplifiers, respectively. While the TWPA decreases the measurement time required for accurate characterization at single-photon powers circulating in the resonators, the largest probe signals would saturate it. We thus turn the pump tone off at high probe powers and verify that the internal quality factors extracted at intermediate powers are the same with the pump tone ON and OFF.

### C. EXTRACTION OF THE INTERNAL QUALITY FACTOR

In this manuscript, we have used the open source fitting routine of [38] to extract the quality factors from the measured data. For resonators in the hanger configuration, the model for the transmitted signal  $S_{21}(f)$  reads

$$S_{21}(f) = ae^{i\alpha}e^{-2\pi if\tau} \left[ 1 - \frac{\frac{Q}{|Q_e|}e^{i\phi}}{1 + 2iQ\left(\frac{f}{f_r} - 1\right)} \right]. \quad (2)$$

The term in front of the brackets covers contributions from the measurement environment where  $a$  describes the baseline level of transmission,  $\alpha$  the phase shift, and  $\tau$  the electrical delay across the measurement line.  $f$  is the probe and  $f_r$  the resonance frequency. The model is based on the diameter correction method of [44] where the complex coupling quality factor

$$Q_e = |Q_e|e^{-i\phi} \quad (3)$$

where magnitude  $|Q_e|$  and rotation angle  $-\phi$  accounts for asymmetries in the Lorentzian shape, e.g., due to impedance mismatch between the resonator and feedline, or the feedline and the measurement environment [44], [45]. The loaded quality factor  $Q$  is then given by

$$Q^{-1} = Q_i^{-1} + Q_c^{-1} \quad (4)$$

where

$$Q_c^{-1} = \Re \left\{ Q_e^{-1} \right\} \quad (5)$$

and  $Q_i$  is the internal quality factor.

Following the circuit analysis of [46] and [47], the root mean square voltage  $V_r$  of the standing wave inside a hanger type CPW resonator at resonance is given by

$$V_r = Q\sqrt{\frac{2Z_r}{\pi Q_c} \left(\frac{l}{\lambda}\right)^{-1} P_{\text{dev}}} \quad (6)$$

with the characteristic impedance  $Z_r$  of the resonator's CPW.  $\lambda$  is the wavelength at resonance,  $l$  is the length of the resonator, and  $P_{\text{dev}}$  is the power entering the DUT. This equation is valid for both quarter- and half-wave resonators and their higher frequency modes as well. The average energy  $E$  inside such CPW resonator is given by

$$E = \frac{1}{2f_r Z_r} \frac{l}{\lambda} V_r^2. \quad (7)$$

Thus, with (6) and (7), we calculate the average number of photons circulating in the resonator in accordance with [48]

as

$$n_{\text{ph}} = \frac{E}{hf_r} = \frac{1}{\pi} \frac{Q^2 P_{\text{dev}}}{Q_c hf_r^2} \quad (8)$$

where  $h$  is Planck's constant. We estimate  $P_{\text{dev}}$  from the output power at the room-temperature generator as described in Appendix B-B. Note that (8) is valid for any resonator in hanger configuration. However, in a one-port reflection measurement, the right-hand side of the equation would be multiplied by a factor of 2. In the  $Q_i$  histograms of Figs. 2 and 4 of the main text, we show for each resonator, the mean  $Q_i$  from all measurements with  $n_{\text{ph}} < 5$ .

The TSV terminations of the devices shown in Fig. 3 of the main text represent the shorted end of the quarter-wave resonators and are therefore located at the current maxima of the standing waves. Thus, for  $l = \lambda/4$ , the maximum current flowing through the TSV terminations can be estimated from

$$\hat{I}_{\text{TSV}} = \sqrt{2} \frac{V_r}{Z_r} = 4Q \sqrt{\frac{P_{\text{dev}}}{\pi Q_c Z_r}} \quad (9)$$

with  $Z_r = 50 \Omega$ .

## ACKNOWLEDGMENT

The authors would like to acknowledge Jan Toivonen, Harri Pohjonen, Ville Selinmaa, Paula Holmlund, and Jaana Marles for technical assistance. K. Grigoras led process development of via etching and ALD and was a key contributor to electrode and membrane layer development. N. Yurttagül and J.-P. Kaikkonen led process development of the electrode and membrane layers. E. T. Mannila led characterization and analysis efforts together with N. Tiencken. P. Eskelinen led process development of the final ALD recipe. A. Ronzani, J. Hättinen, and S. Simbierowicz contributed to dc characterization throughout the process development. S. Simbierowicz also contributed to mask design. L. Grönberg, V. Vesterinen, and S. Simbierowicz contributed to development of relevant planar resonators. D. Datta and V. Vesterinen contributed to RF measurements. D. P. Lozano did process development of electrode layer deposition and device characterization at Chalmers, used in earlier iterations of the devices that the reported devices improve upon. H.-X. Li contributed to device characterization. M. Rommel contributed to process development. D. Shiri contributed to microwave design and analysis. J. Biznárová, A. Fadavi Roudsari, S. Kosen, and A. Osman assisted in fabrication, characterization, and discussions. J. Bylander supervised the work at Chalmers. J. Govenius supervised and contributed technical advice to all aspects of the work, after the first phases were supervised and planned by M. Prunnila and J. Hassel.

## REFERENCES

- [1] I. Chiorescu, Y. Nakamura, C. J. P. M. Harmans, and J. E. Mooij, "Coherent quantum dynamics of a superconducting flux qubit," *Science*, vol. 299, no. 5614, pp. 1869–1871, 2003, doi: [10.1126/science.108110](https://doi.org/10.1126/science.108110).

- [2] A. P. M. Place et al., "New material platform for superconducting transmon qubits with coherence times exceeding 0.3 milliseconds," *Nat. Commun.*, vol. 12, no. 1, Dec. 2021, Art. no. 1779, doi: [10.1038/s41467-021-22030-5](https://doi.org/10.1038/s41467-021-22030-5).
- [3] C. Wang et al., "Towards practical quantum computers: Transmon qubit with a lifetime approaching 0.5 milliseconds," *NPJ Quantum Inf.*, vol. 8, no. 1, pp. 1–6, 2022, doi: [10.1038/s41534-021-00510-2](https://doi.org/10.1038/s41534-021-00510-2).
- [4] R. T. Gordon et al., "Environmental radiation impact on lifetimes and quasiparticle tunneling rates of fixed-frequency transmon qubits," *Appl. Phys. Lett.*, vol. 120, no. 7, 2022, Art. no. 074002, doi: [10.1063/5.0078785](https://doi.org/10.1063/5.0078785).
- [5] A. Somoroff, Q. Ficheux, R. A. Mencia, H. Xiong, R. V. Kuzmin, and V. E. Manucharyan, "Millisecond coherence in a superconducting qubit," 2021, *arXiv:2103.08578*, doi: [10.48550/arXiv.2103.08578](https://doi.org/10.48550/arXiv.2103.08578).
- [6] A. G. Fowler, M. Mariantoni, J. M. Martinis, and A. N. Cleland, "Surface codes: Towards practical large-scale quantum computation," *Phys. Rev. A*, vol. 86, no. 3, Sep. 2012, Art. no. 032324, doi: [10.1103/PhysRevA.86.032324](https://doi.org/10.1103/PhysRevA.86.032324).
- [7] M. Reiher, N. Wiebe, K. M. Svore, D. Wecker, and M. Troyer, "Elucidating reaction mechanisms on quantum computers," *Proc. Nat. Acad. Sci.*, vol. 114, no. 29, pp. 7555–7560, Jul. 2017, doi: [10.1073/pnas.1619152114](https://doi.org/10.1073/pnas.1619152114).
- [8] S. B. Bravyi and A. Y. Kitaev, "Quantum codes on a lattice with boundary," Nov. 1998, *arXiv:quant-ph/9811052*, doi: [10.48550/arXiv.quant-ph/9811052](https://doi.org/10.48550/arXiv.quant-ph/9811052).
- [9] F. Arute et al., "Quantum supremacy using a programmable superconducting processor," *Nature*, vol. 574, no. 7779, pp. 505–510, Oct. 2019, doi: [10.1038/s41586-019-1666-5](https://doi.org/10.1038/s41586-019-1666-5).
- [10] Y. Wu et al., "Strong quantum computational advantage using a superconducting quantum processor," *Phys. Rev. Lett.*, vol. 127, Oct. 2021, Art. no. 180501, doi: [10.1103/PhysRevLett.127.180501](https://doi.org/10.1103/PhysRevLett.127.180501).
- [11] P. Jurcevic et al., "Demonstration of quantum volume 64 on a superconducting quantum computing system," *Quantum Sci. Technol.*, vol. 6, no. 2, Mar. 2021, Art. no. 025020, doi: [10.1088/2058-9565/abe519](https://doi.org/10.1088/2058-9565/abe519).
- [12] J. M. Gambetta et al., "Investigating surface loss effects in superconducting transmon qubits," *IEEE Trans. Appl. Supercond.*, vol. 27, no. 1, pp. 1–5, Jan. 2017, doi: [10.1109/TASC.2016.2629670](https://doi.org/10.1109/TASC.2016.2629670).
- [13] A. Dunsworth et al., "Characterization and reduction of capacitive loss induced by sub-micron Josephson junction fabrication in superconducting qubits," *Appl. Phys. Lett.*, vol. 111, no. 2, 2017, Art. no. 22601, doi: [10.1063/1.4993577](https://doi.org/10.1063/1.4993577).
- [14] A. Nersisyan et al., "Manufacturing low dissipation superconducting quantum processors," in *IEEE Int. Electron Devices Meeting*, 2019, pp. 31.1.1–31.1.4, doi: [10.1109/IEDM19573.2019.8993458](https://doi.org/10.1109/IEDM19573.2019.8993458).
- [15] J. J. Burnett et al., "Decoherence benchmarking of superconducting qubits," *NPJ Quantum Inf.*, vol. 5, no. 1, pp. 1–8, Dec. 2019, doi: [10.1038/s41534-019-0168-5](https://doi.org/10.1038/s41534-019-0168-5).
- [16] A. Osman et al., "Simplified Josephson-junction fabrication process for reproducibly high-performance superconducting qubits," *Appl. Phys. Lett.*, vol. 118, no. 6, Feb. 2021, Art. no. 064002, doi: [10.1063/5.0037093](https://doi.org/10.1063/5.0037093).
- [17] S. Kosen et al., "Building blocks of a flip-chip integrated superconducting quantum processor," *Quantum Sci. Technol.*, vol. 7, no. 3, Jun. 2022, Art. no. 035018, doi: [10.1088/2058-9565/ac734b](https://doi.org/10.1088/2058-9565/ac734b).
- [18] J. Wenner et al., "Wirebond crosstalk and cavity modes in large chip mounts for superconducting qubits," *Supercond. Sci. Technol.*, vol. 24, no. 6, Jun. 2011, Art. no. 065001, doi: [10.1088/0953-2048/24/6/065001](https://doi.org/10.1088/0953-2048/24/6/065001).
- [19] S. K. Tolpygo, V. Bolkhovskiy, T. Weir, L. M. Johnson, W. D. Oliver, and M. A. Gouker, "Deep sub-micron stud-via technology of superconductor VLSI circuits," *Supercond. Sci. Technol.*, vol. 27, no. 2, Jan. 2014, Art. no. 025016, doi: [10.1088/0953-2048/27/2/025016](https://doi.org/10.1088/0953-2048/27/2/025016).
- [20] M. Kiviranta et al., "Multilayer fabrication process for Josephson junction circuits cross-compatible over two foundries," *IEEE Trans. Appl. Supercond.*, vol. 26, no. 6, pp. 1–5, Sep. 2016, Art. no. 1100905, doi: [10.1109/TASC.2016.2544821](https://doi.org/10.1109/TASC.2016.2544821).
- [21] D. R. W. Yost et al., "Solid-state qubits integrated with superconducting through-silicon vias," *NPJ Quantum Inf.*, vol. 6, no. 1, pp. 1–7, Dec. 2020, doi: [10.1038/s41534-020-00289-8](https://doi.org/10.1038/s41534-020-00289-8).
- [22] J. L. Mallek et al., "Fabrication of superconducting through-silicon vias," Mar. 2021, *arXiv:2103.08536*, doi: [10.48550/arXiv.2103.08536](https://doi.org/10.48550/arXiv.2103.08536).
- [23] C. R. H. McRae et al., "Materials loss measurements using superconducting microwave resonators," *Rev. Sci. Instrum.*, vol. 91, no. 9, Sep. 2020, Art. no. 091101, doi: [10.1063/5.0017378](https://doi.org/10.1063/5.0017378).

- [24] C. T. Earnest et al., "Substrate surface engineering for high-quality silicon/aluminum superconducting resonators," *Supercond. Sci. Technol.*, vol. 31, no. 12, Dec. 2018, Art. no. 125013, doi: [10.1088/1361-6668/aae548](https://doi.org/10.1088/1361-6668/aae548).
- [25] J. Burnett, A. Bengtsson, D. Niepce, and J. Bylander, "Noise and loss of superconducting aluminium resonators at single photon energies," *J. Phys.: Conf. Ser.*, vol. 969, Mar. 2018, Art. no. 012131, doi: [10.1088/1742-6596/969/1/012131](https://doi.org/10.1088/1742-6596/969/1/012131).
- [26] G. Calusine et al., "Analysis and mitigation of interface losses in trenched superconducting coplanar waveguide resonators," *Appl. Phys. Lett.*, vol. 112, no. 6, Feb. 2018, Art. no. 062601, doi: [10.1063/1.5006888](https://doi.org/10.1063/1.5006888).
- [27] M. V. P. Altoé et al., "Localization and reduction of superconducting quantum coherent circuit losses," Dec. 2020, *arXiv:2012.07604*, doi: [10.48550/arXiv.2012.07604](https://doi.org/10.48550/arXiv.2012.07604).
- [28] J. Verjaaw et al., "Investigation of microwave loss induced by oxide re-growth in high-Q niobium resonators," *Phys. Rev. Appl.*, vol. 16, no. 1, Jul. 2021, Art. no. 014018, doi: [10.1103/PhysRevApplied.16.014018](https://doi.org/10.1103/PhysRevApplied.16.014018).
- [29] C. A. Jhavalala et al., "Kilopixel backshort-under-grid arrays for the primordial inflation polarization explorer," in *Millimeter, Submillimeter, and Far-Infrared Detectors and Instrumentation for Astronomy*, vol. 9153, W. S. Holland and J. Zmuidzinas, Eds. Bellingham, WA, USA: International Society for Optics and Photonics, SPIE, 2014, pp. 1038–1048, doi: [10.1117/12.2056995](https://doi.org/10.1117/12.2056995).
- [30] M. Vahidpour et al., "Superconducting through-silicon vias for quantum integrated circuits," Aug. 2017, *arXiv:1708.02226*, doi: [10.48550/arXiv.1708.02226](https://doi.org/10.48550/arXiv.1708.02226).
- [31] J. A. Alfaro-Barrantes et al., "Highly-conformal sputtered through-silicon vias with sharp superconducting transition," *J. Microelectromech. Syst.*, vol. 30, no. 2, pp. 253–261, 2021, doi: [10.1109/JMEMS.2021.3049822](https://doi.org/10.1109/JMEMS.2021.3049822).
- [32] F. Laermer and A. Schilp, "Method of anisotropically etching silicon," US Patent 5 501 893, Mar. 1996.
- [33] B. Wu, A. Kumar, and S. Pamarthy, "High aspect ratio silicon etch: A review," *J. Appl. Phys.*, vol. 108, no. 5, p. 9, Sep. 2010, doi: [10.1063/1.3474652](https://doi.org/10.1063/1.3474652).
- [34] V. E. Manucharyan, J. Koch, L. I. Glazman, and M. H. Devoret, "Fluxonium: Single Cooper-pair circuit free of charge offsets," *Science*, vol. 326, no. 5949, pp. 113–116, 2009, doi: [10.1126/science.11755](https://doi.org/10.1126/science.11755).
- [35] W. Woods et al., "Determining interface dielectric losses in superconducting coplanar-waveguide resonators," *Phys. Rev. Appl.*, vol. 12, no. 1, Jul. 2019, Art. no. 014012, doi: [10.1103/PhysRevApplied.12.014012](https://doi.org/10.1103/PhysRevApplied.12.014012).
- [36] V. Lahtinen and M. Möttönen, "Effects of device geometry and material properties on dielectric losses in superconducting coplanar-waveguide resonators," *J. Phys.: Condens. Matter*, vol. 32, no. 40, Sep. 2020, Art. no. 405702, doi: [10.1088/1361-648X/ab98c8](https://doi.org/10.1088/1361-648X/ab98c8).
- [37] D. Niepce, J. J. Burnett, M. G. Latorre, and J. Bylander, "Geometric scaling of two-level-system loss in superconducting resonators," *Supercond. Sci. Technol.*, vol. 33, no. 2, Jan. 2020, Art. no. 025013, doi: [10.1088/1361-6668/ab6179](https://doi.org/10.1088/1361-6668/ab6179).
- [38] S. Probst, F. Song, P. A. Bushev, A. V. Ustinov, and M. Weides, "Efficient and robust analysis of complex scattering data under noise in microwave resonators," *Rev. Sci. Instrum.*, vol. 86, no. 2, 2015, Art. no. 024706, doi: [10.1063/1.4907935](https://doi.org/10.1063/1.4907935).
- [39] I. Bahl, M. Bozzi, and R. Garg, "Coplanar lines: Coplanar waveguides and coplanar strips," in *Microstrip Lines and Slotlines*, 3rd ed. Norwood, MA, USA: Artech House, 2013, pp. 347–432.
- [40] J. Krupka, J. Breeze, A. Centeno, N. Alford, T. Claussen, and L. Jensen, "Measurements of permittivity, dielectric loss tangent, and resistivity of float-zone silicon at microwave frequencies," *IEEE Trans. Microw. Theory Techn.*, vol. 54, no. 11, pp. 3995–4001, Nov. 2006, doi: [10.1109/TMTT.2006.883655](https://doi.org/10.1109/TMTT.2006.883655).
- [41] J. G. C. Milne, "Superconducting transition temperature of high-purity tantalum metal," *Phys. Rev.*, vol. 122, no. 2, pp. 387–388, Apr. 1961, doi: [10.1103/PhysRev.122.387](https://doi.org/10.1103/PhysRev.122.387).
- [42] A. Torgovkin, S. Chaudhuri, A. Ruhtinas, M. Lahtinen, T. Sajavaara, and I. J. Maasilta, "High quality superconducting titanium nitride thin film growth using infrared pulsed laser deposition," *Supercond. Sci. Technol.*, vol. 31, no. 5, May 2018, Art. no. 055017, doi: [10.1088/1361-6668/aab7d6](https://doi.org/10.1088/1361-6668/aab7d6).
- [43] J. Gao, "The physics of superconducting microwave resonators," Ph.D. dissertation, California Inst. Technol., Pasadena, CA, USA, 2008, doi: [10.7907/RAT0-VM75](https://doi.org/10.7907/RAT0-VM75).
- [44] M. S. Khalil, M. J. A. Stoutimore, F. C. Wellstood, and K. D. Osborn, "An analysis method for asymmetric resonator transmission applied to superconducting devices," *J. Appl. Phys.*, vol. 111, no. 5, 2012, Art. no. 54510, doi: [10.1063/1.3692073](https://doi.org/10.1063/1.3692073).
- [45] C. Deng, M. Otto, and A. Lupascu, "An analysis method for transmission measurements of superconducting resonators with applications to quantum-regime dielectric-loss measurements," *J. Appl. Phys.*, vol. 114, no. 5, Aug. 2013, Art. no. 054504, doi: [10.1063/1.4817512](https://doi.org/10.1063/1.4817512).
- [46] R. Barends, "Photon-detecting superconducting resonators," Ph.D. dissertation, Delft Univ. Technol., Delft, The Netherlands, 2009. [Online]. Available: <https://www.narcis.nl/publication/RecordID/oa:i:tu-delft.nl:uuiid:574944e6-c3ce-4c86-a511-a88385b22379>
- [47] P. J. De Visser, "Quasiparticle dynamics in aluminium superconducting microwave resonators," Ph.D. dissertation, Delft Univ. Technol., Delft, Netherlands, 2014, doi: [10.4233/uuiid:cae4c9fc-f90d-4c12-a878-8428ee4adb4c](https://doi.org/10.4233/uuiid:cae4c9fc-f90d-4c12-a878-8428ee4adb4c).
- [48] A. Bruno, G. de Lange, S. Asaad, K. L. van der Enden, N. K. Langford, and L. DiCarlo, "Reducing intrinsic loss in superconducting resonators by surface treatment and deep etching of silicon substrates," *Appl. Phys. Lett.*, vol. 106, no. 18, 2015, Art. no. 182601, doi: [10.1063/1.4919761](https://doi.org/10.1063/1.4919761).